eNeuro

MRI Compatible, Customizable, and 3D Printable Microdrive for Neuroscience Research

This Early Release article has been peer-reviewed and accepted, but has not been through the composition and copyediting processes. The final version may differ slightly in style or formatting and will contain links to any extended data.

Alerts: Sign up at www.eneuro.org/alerts to receive customized email alerts when the fully formatted version of this article is published.

1   **MRI Compatible, Customizable, and 3D Printable Microdrive for Neuroscience Research**

2   Abbreviated Title: **MRI Compatible and Customizable Microdrive**

3   Eunha Baeg [1,2,†] , Raymond Doudlah[3,†] , Robert Swader[4] , Hyowon Lee[5] , Minjun Han[2] , Seong-Gi Kim[1,2] ,

4   Ari Rosenberg[3] , and Byounghoon Kim[3]

5   [1] Center for Neuroscience Imaging Research, Institute for Basic Science, Suwon, Republic of Korea

6   [2] Department of Biomedical Engineering, Sungkyunkwan University, Suwon, Republic of Korea

7   [3] Department of Neuroscience, School of Medicine and Public Health, University of Wisconsin – Madison,

8   Madison, WI. 53705, USA

9   [4] Morgridge Institute for Research, Madison, WI. 53705, USA

10   [5] System Design Engineering, University of Waterloo, Waterloo, ON., Canada

11   [†]Equal Contributions

12

13   **Author contributions**: E.B., A.R., and B.K. designed research; R.D., R.S., H.L., and B.K. CAD design and

14   fabrication; E.B., M.H., S.G.K., and B.K. performed the experiments; E.B., M.H., and B.K. analyzed data;

15   E.B., R.D., A.R., and B.K. wrote the paper.

16   **Correspondence should be addressed to:**

17   Byounghoon Kim Department of Neuroscience School of Medicine and Public Health University of

18   Wisconsin – Madison 1111 Highland Ave. WIMR-II, Office 5505 Madison, WI. 53705 Email:

19   bkim10@wisc.edu

20

21   **Number of Figures:** 8

22   **Number of Tables:** 1

23   **Number of words in the Abstract:** 237

24   **Number of words in the Significance Statement:** 116

25   **Number of words in the Introduction:** 499

26   **Number of words in the Materials and Methods:** 2752

27   **Number of words in the Results:** 419

28   **Number of words in the Discussion:** 710

29   **Conflict of Interest:** The authors declare no competing financial interests.

1

35   **Abstract**

36   The effective connectivity of brain networks can be assessed using functional magnetic

37   resonance imaging (fMRI) to quantify the effects of local electrical microstimulation (EM) on

38   distributed neuronal activity. The delivery of EM to specific brain regions, particularly with layer

39   specificity, requires MRI compatible equipment that provides fine control of a stimulating

40   electrode's position within the brain while minimizing imaging artifacts. To this end, we

41   developed a microdrive made entirely of MRI compatible materials. The microdrive uses an

42   integrated penetration grid to guide electrodes and relies on a micro-drilling technique to

43   eliminate the need for large craniotomies, further reducing implant maintenance and image

44   distortions. The penetration grid additionally serves as a built-in MRI marker, providing a visible

45   fiducial reference for estimating probe trajectories. Following the initial implant procedure, these

46   features allow for multiple electrodes to be inserted, removed, and repositioned with minimal

47   effort, using a screw-type actuator. To validate the design of the microdrive, we conducted an

48   EM-coupled fMRI study with a male macaque monkey. The results verified that the microdrive

49   can be used to deliver EM during MRI procedures with minimal imaging artifacts, even within a

50   7 Tesla (7T) environment. Future applications of the microdrive include neuronal recordings and

51   targeted drug delivery. We provide computer aided design (CAD) templates and a parts list for

52   modifying and fabricating the microdrive for specific research needs. These designs provide a

53   convenient, cost-effective approach to fabricating MRI compatible microdrives for neuroscience

54   research.

55

56   **Key words:** microdrive; MRI compatible; electrical microstimulation; electrophysiology; effective

57   connectivity; 3D printing.

58

59   **Significance Statement**

60   We provide designs for a customizable, MRI compatible microdrive capable of positioning

61   various types of probes (e.g., stimulating electrodes, recording electrodes, drug cannulae, or

62   optogenetic fibers) within the brain. The design integrates a cranial implant, penetration grid for

63   guiding probes, and a microdrive body assembly with actuators. A micro-drilling technique,

64   which helps reduce implant maintenance and potential imaging artifacts, is described for

65   introducing probes into the brain. Our open-source designs allow for the customization and

66   fabrication of microdrive components to meet the unique demands of specific research projects

67   and various animal models. Microdrives based on these designs can fulfill a variety of research

68   needs within the neuroscience community related to electrical microstimulation, neuronal

69   recording, and local drug delivery.

Introduction

71 Hemodynamic responses measured using functional magnetic resonance imaging (fMRI) can
72 be used to study the organization of brain networks (Ogawa & Lee, 1990; Kourtzi et al., 2003;
73 Logothetis, 2003). In particular, fMRI signals evoked by local electrical microstimulation (EM)
74 can reveal the effective connectivity of different brain areas (Tolias et al., 2005; Logothetis et al.,
75 2010; Premereur et al., 2015; Dromme et al., 2016; Duffau, 2020; Premereur & Janssen, 2020).
76 An MRI compatible microdrive capable of positioning various types of probes (e.g., stimulating
77 electrodes, recording electrodes, drug cannulae, or optogenetic fibers) can facilitate a variety of
78 fMRI-based studies. Indeed, incorporating neuromodulation approaches, such as EM and
79 pharmacological methods, into non-human primate neuroimaging studies was recently identified
80 as a five year goal of "unprecedented value" (Milham et al., 2020).

81 Currently, relatively few commercially or academically available microdrives can support
82 this goal (**Table 1**), and several factors limit discovery. First, long travel distances may be
83 required to reach a desired brain region. For example, more than 30 mm of travel is required to
84 reach some ventral brain regions in macaques. However, only a few available MRI compatible
85 microdrives can travel such long distances. Second, a scanner's bore size can preclude the use
86 of stereotactic manipulators due to the length of the electrode holders. Third, electrode holders
87 can amplify mechanical vibrations from the scanner, resulting in tissue and/or probe damage.
88 Frameless, skull-mounted microdrives provide effective solutions to problems of bore size and
89 mechanical vibrations but generally have limited travel distance (Wilson et al., 2003; Greenberg
90 & Wilson, 2004). To reduce duplicated efforts associated with groups developing their own
91 microdrives *de novo* (Moeller et al., 2008; McMahon et al., 2014) and facilitate discovery, we
92 designed a novel MRI compatible microdrive that can be customized to support a wide range of
93 experimental needs.

94 Here we present a frameless, skull-mounted MRI compatible microdrive that
95 encapsulates a cranial implant, penetration grid, and actuating mechanism capable of
96 positioning various types of probes over long travel distances. To minimize imaging artifacts, all
97 components are MRI compatible. The penetration grid used in conjunction with a contrast agent
98 is visible in structural scans, providing a fiducial reference for estimating penetration trajectories
99 (Kalwani et al., 2009; Dubowitz & Scadeng, 2011; Glud et al., 2017). The penetration grid
100 further serves as a guide for a micro-drilling technique that replaces conventional craniotomies
101 with small holes through which probes are introduced into the brain (Rosenberg et al., 2013;
102 Laurens et al., 2016; Chang et al., 2020). Compared to conventional craniotomies and
103 chambers, this technique reduces potential artifacts caused by air-filled spaces, the need for

104 periodic debridement of granulation tissue, and potential deformation of the underlying neuronal
105 tissue (Wilson et al., 2005; Spitler & Gothard, 2008; Premereur & Janssen, 2020).

106   We tested the microdrive by using it to introduce a stimulating electrode into the striatum
107 of a macaque monkey and delivered EM during an fMRI session in a 7 Tesla (7T) scanner.
108 Cerebral blood volume (CBV) with monocrystalline iron oxide nanoparticles (MION) was used to
109 measure the effects of the delivered EM (Vanduffel et al., 2001; Kim et al., 2013). We provide
110 computer aided design (CAD) files to facilitate modification and fabrication (https://osf.io/tnpmk;
111 RRID:SCR_019247), such as adding/removing actuators and scaling components to
112 accommodate different animal models. We anticipate that this cost-effective, customizable
113 microdrive can support a wide range of neuroscience research requiring fine probe positioning.

114

115 **Table 1.** Example MRI compatible microdrives.

| Availability	Manufacturer/Source	Construction style	Actuating mechanism	Electrode travel distance	Craniotomy required
Commercial	NeuroNexus, Inc. (MRI-compatible matrix array)	stand-alone	N/A	fixed length (max 15 mm)	yes
Commercial	FHC, Inc. (NeuroPace)	stand-alone	N/A	fixed length based on electrode	no
Commercial	NaN Instruments, Inc. (NAN MRI drive)	tower style	motorized screw type	max: 120 mm	yes
Academic	Kern et al. (2008)	stand-alone	ultrasonic actuator	max: 50 mm	yes
Academic	Grahn et al. (2016)	frame-based stereotactic system	manual screw type	max: 12 mm	yes
Academic	Dotson et al. (2017)	stand-alone	manual screw type	max: 20 mm	yes
Academic	Sudhakar et al. (2019)	stand-alone	N/A	fixed length based on electrode	yes

116

Materials and Methods

Microdrive architecture and design

119 The microdrive consists of two major components: (1) the implant and penetration grid, and (2)
120 the microdrive body assembly (**Fig. 1A**). The implant is fixed to the cranium and serves as an
121 anchor frame for attaching the penetration grid and microdrive body assembly (**Fig. 1B**). The
122 penetration grid provides a coordinate system for planning trajectories to reach specific brain
123 areas and guides micro-drilling for the insertion of guide tubes which protect the probes (e.g.,

5

124 stimulating electrodes, recording electrodes, drug cannulae, optogenetic fibers, etc.). In the

125 presented design, the microdrive body assembly contains four chambers which align with the

126 four quadrants of the penetration grid. Each chamber houses an individual actuator that

127 independently controls a single probe (**Fig. 1C**).

128

129
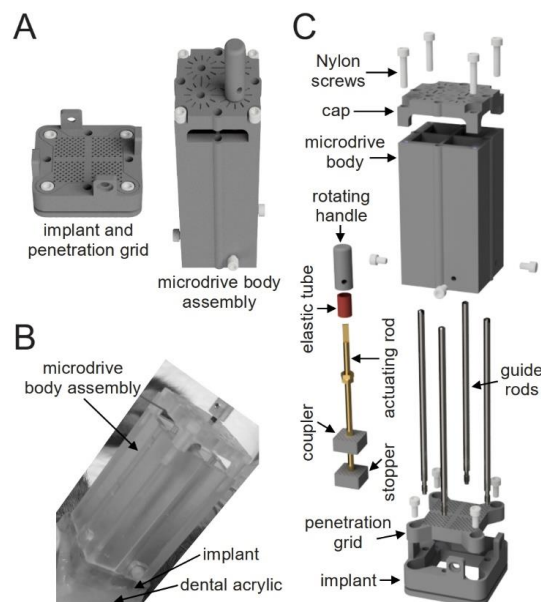
130 **Figure 1.** Overview of the microdrive design. ***A***, 3D rendering of the two major components of
131 the microdrive: (1) implant and penetration grid (left) and (2) microdrive body assembly (right). ***B***,
132 Picture of a 3D printed microdrive body assembly installed on an implant that is fixed to a layer
133 of dental acrylic on the cranium of a macaque monkey. ***C***, Exploded view of the microdrive to
134 visualize the components and their assembly. All components are described in detail in the
135 following sections and figures. CAD files and a parts list for all components are available for
136 download (https://osf.io/tnpmk).

137

138 CAD files for all parts and assemblies were created using SolidWorks (Dassault

139 Systèmes, SolidWorks Corporation). A Viper si2 SLA System (3D Systems, Inc.) with 0.0025

140 mm vertical resolution and 0.075 mm beam diameter was used for 3D printing. All 3D printed

141 components were made of Accura 60 photopolymer resin (3D Systems, Inc.), which was

142 selected for its chemical resistance and mechanical durability (tensile strength: 5868 MPa;

143 tensile modulus: 2,600 – 3,100 MPa). Where necessary, 3D printed parts were manually

144 threaded with a standard 2-56 tap (56 threads per inch with a pitch of 453 μm) with the aid of a

145 manual mill to maintain alignment. The actuating rod and guide rods (**Fig. 1C**) were not 3D

146 printed and required minor machining (as discussed below).

6

147

148   *Implant and penetration grid*

149   The implant is a square frame (29 x 29 mm) with four vertical tongues for securing the

150   microdrive body assembly (**Fig. 2A**) and a threaded hole on each edge for securing guide rods

151   (**Fig. 2B** yellow circles). The guide rods are used to align the microdrive body assembly and

152   implant during installation and removal, thereby preventing damage to the guide tubes and/or

153   probes (**Fig. 1C**; also see Figure 6D). These rods were made of MRI compatible 3/32" grade 5

154   titanium alloy and were turned on a lathe. To reduce image distortion, the guide rods can be

155   unscrewed and removed after the microdrive body assembly has been secured to the implant.

156   The outer surface of the implant contains a groove (**Fig. 2A** black arrow) which serves as an

157   embedding space when securing the implant to the cranium with dental acrylic (described

158   below).

159

160
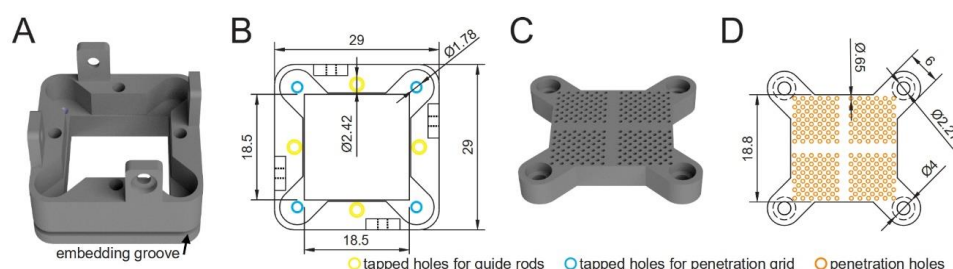
Figure 2. Implant and penetration grid. **A**, 3D rendering of the implant. To help secure the
implant to the cranium, the outer surface includes a groove (black arrow) which provides an
embedding space for dental acrylic. Four vertical tongues are used to secure the microdrive
body to the implant with Nylon screws. The cutout houses the penetration grid. **B**, Top-view line
drawing of the implant with dimensions. Tapped holes on each edge secure the guide rods
(yellow circles). **C**, 3D rendering of the penetration grid. **D**, Top-view line drawing of the
penetration grid with dimensions. The penetration grid is secured to the implant using Nylon
screws (blue circles in **B**). Each quadrant contains penetration holes (orange circles) which are
used to estimate probe trajectories and guide micro-drilling. Dimensions are in mm.

170

171   The main portion of the penetration grid is square in shape with anchor points in each

172   corner that fit into the cutout of the implant (**Fig. 2C**,**D**). It is secured to the implant using four

173   Nylon screws (**Fig. 2B** blue circles). The grid has four quadrants, each with 61 penetration holes

174   (**Fig. 2D** orange circles; ϕ0.65 mm), providing a coordinate system for planning trajectories and

175   guiding micro-drilling for the insertion of guide tubes and probes. The location, number, and size

176   of the holes can be modified based on experimental needs.

177

7

178 *Microdrive body assembly*

179 The microdrive body assembly consists of two main components: (1) the microdrive body and
180 cap, and (2) the actuating mechanism. In the presented design, the microdrive body contains
181 four chambers (**Fig. 3A**), each of which can house a single actuating mechanism. The
182 chambers are rectangular (9 x 9 x 45 mm) and align with the four quadrants of the penetration
183 grid (**Figs. 2C**,**D**, **3B**), providing positioning access for probes over a 353 mm^2 area. The bottom
184 corners of each chamber have small stopping notches upon which the stopper of the actuating
185 mechanism sits (**Fig. 3B** orange triangles). This provides a base of support for the actuating
186 mechanism and prevents it from sliding out the bottom of the chamber. Each face of the
187 microdrive body contains a slot along its length for a guide rod (**Fig. 3B** red circles, **Fig. 3C** red
188 lines). These rods align the microdrive body assembly with the penetration grid and implant in
189 order to reduce the risk of damaging guide tubes or probes when installing/removing the
190 microdrive body assembly onto/from the implant (see Figure 6D). Nylon screws are used to
191 secure the microdrive body to the implant via tapped holes on each face of the body (**Fig. 3B**
192 green lines, **Fig. 3C** green circles and lines) which align with the tongues on the implant (**Fig.**
193 **2A**,**B**). The microdrive cap (**Figs. 1C**, **3D**, **4A**) holds and aligns the actuating mechanisms within
194 the chambers of the microdrive body (**Fig. 3D** blue circles, **Fig. 4A**). The cap also has
195 measurement indicators for tracking the rotation of the actuating rods (**Fig. 3D** marks extending
196 radially from each actuating rod hole). The top of the microdrive body contains tapped holes in
197 each corner for securing the cap with Nylon screws (**Fig. 3B** purple circles, **Fig. 3C** purple lines).
198
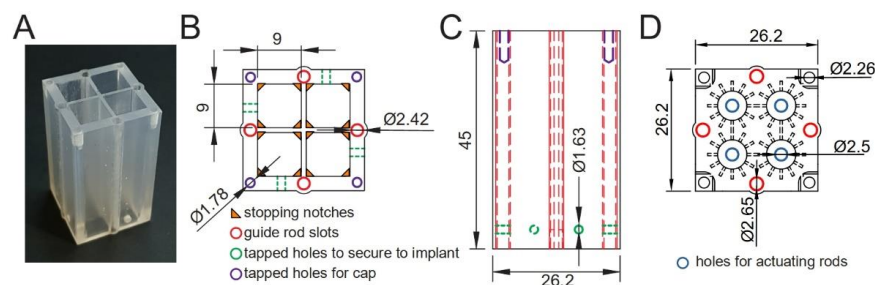
199

200 **Figure 3.** Microdrive body and cap. **A**, Picture of a 3D printed microdrive body with four
201 chambers. Each chamber can house an independently controlled probe. **B**, Top-view line
202 drawing of the microdrive body with dimensions. Slots on each edge (red circles) fit over the
203 guide rods to align the microdrive body with the implant and penetration grid. **C**, Side-view line
204 drawing of the microdrive body with dimensions. Red lines show the guide rod slots. The
205 microdrive body secures to the implant via tapped holes on the bottom of each face (green
206 lines/circles in **B**,**C**). **D**, Top-view line drawing of the microdrive cap with dimensions. When the
207 cap is installed, the ends of the actuating rods slide through holes in the cap (blue circles),

208 exposing enough of the rods to secure rotating handles. The marks extending radially out from
209 the actuating rod holes are indices for tracking the rotation of the actuating rods. The microdrive
210 cap secures to the microdrive body via tapped holes (purple circles/lines in **B**,**C**) using Nylon
211 screws. Dimensions are in mm.

212

213 The actuating mechanism, which raises and lowers the probe, consists of three parts: (1)
214 a threaded actuating rod, (2) stopper, and (3) coupler (**Fig. 4A**). The actuating rod has a
215 scalloped end (**Fig. 4B** bottom) that inserts into a latching slot in the center of the stopper (**Fig.**
216 **4C**). The stopper is square and fits snuggly within a chamber of the microdrive body. When an
217 actuating mechanism is assembled and loaded into a chamber, the stopper sits on stopping
218 notches at the bottom of the chamber to prevent the actuating mechanism from sliding out
219 through the bottom of the microdrive body (**Fig. 3B** orange triangles; also see Figure 6C). The
220 coupler fits within the chamber above the stopper and additionally threads onto the actuating
221 rod in order to control the position of an attached probe (**Fig. 4D**). Because the coupler fits
222 squarely within the chamber, rotating the actuating rod does not rotate the coupler. Instead, the
223 rotation is converted into vertical translation via a screw and nut mechanism. The stopper
224 provides an anchor point for the actuating rod and coupler that allows the actuating rod to freely
225 rotate because of the latching slot (**Fig. 4A**). In the presented design, the actuating rod and
226 coupler are threaded for 56 threads per inch, which lowers the coupler and attached probe 453
227 µm for each full counterclockwise turn of the actuating rod (clockwise rotations raise the coupler
228 and probe). A rotating handle (**Fig. 4A**) attaches to the beveled end of the actuating rod (**Fig.**
229 **4B** top) to assist with manual rotations. To prevent unwanted vertical translations of the
230 actuating mechanism within the microdrive body chamber, two brass jam nuts (**Fig. 4B** in blue)
231 are used as an adjustable base to support an elastic tube (**Fig. 4B** in red), which sits between
232 the nuts and the microdrive cap (**Fig. 4A**). This structure mimics a compressed spring that
233 creates downward pressure on the actuating mechanism from the microdrive cap, such that the
234 stopper remains pressed against the stopping notches. Thus, the stopper and stopping notches
235 prevent unwanted downward translations, while the brass nuts, elastic tube, and microdrive cap
236 prevent unwanted upward translations. We made the actuating rods from an MRI compatible 2-
237 56 threaded brass rod. The scalloped and beveled ends were manually machined.

238 Penetration holes in the stopper and coupler (**Fig. 4C**,**D** orange circles) align with
239 corresponding holes in the penetration grid. This alignment defines the penetration trajectory of
240 an attached probe. The number, size, and location of these holes can be modified based on
241 experimental needs. In the presented design, the microdrive can be used to individually control
242 up to four probes simultaneously, one in each chamber. The total travel distance of a probe is

243   determined by the length of the microdrive body and actuating rod (39 mm in this design).

244

245
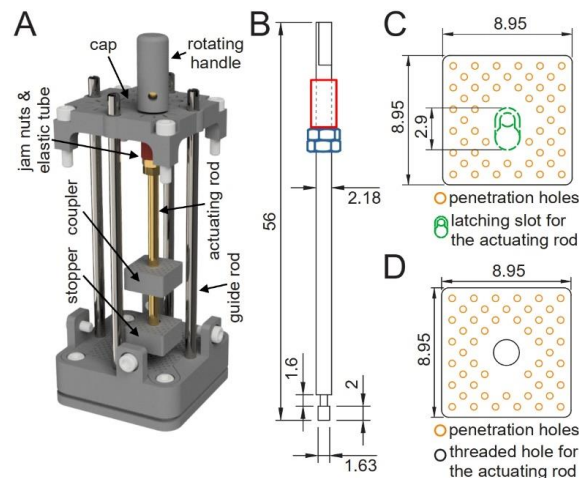
Figure 4. Actuating mechanism. ***A***, 3D rendering of the actuating mechanism, including the actuating rod, stopper, and coupler within the microdrive body (hidden). ***B***, Side-view line drawing of the actuating rod with dimensions. Counterclockwise rotation of the actuating rod advances the probe via the coupler. Jam nuts (in blue) provide an adjustable base to support an elastic tube (in red) which maintains tension between the jam nuts and the microdrive cap to ensure that the actuating mechanism does not inadvertently slide up the microdrive body chamber. The rotating handle attaches to the beveled end of the actuating rod (top). ***C***, Top-view line drawing of the stopper with dimensions. The latching slot (green dashed outline) attaches to the scalloped end of the actuating rod (***B***, bottom), securing the rod during rotations. Penetration holes (orange circles) align with corresponding holes in the coupler and penetration grid. ***D***, Top-view line drawing of the coupler with dimensions. The coupler screws onto the actuating rod via a threaded hole (black circle). This creates a screw and nut mechanism that controls the position of the coupler (and attached probe) by rotating the actuating rod. Penetration holes (orange circles) align with corresponding holes in the stopper and penetration grid (**Fig. 2D**). These holes ensure the positioning and alignment of the guide tube and probe during assembly so that the probe follows the intended trajectory. Dimensions are in mm.

Cranial implant

The implant serves as an anchoring point for the microdrive, so it needs to be secured to the cranium. The implant can be secured directly to the cranium with dental acrylic or to a layer of dental acrylic over the cranium (**Figs. 1B**, **5A**; also see Figure 6A). An advantage of affixing the implant to an acrylic layer, as opposed to the cranium directly, is that it can be readily repositioned within the bounds of the acrylic layer. The outer surface of the implant contains a groove which serves as an embedding space for the dental acrylic (**Fig. 2A** black arrow). Once the acrylic hardens, thus securing the implant, the implant can be protected using a cover that attaches with four Nylon screws (not shown here but included with the CAD files).

272

273

Estimating the penetration trajectory using a fiducial MRI marker

Estimating the trajectory and confirming the position of a probe within the brain is crucial to the success of an experiment but can be challenging without a stereotactic frame. Even with a stereotactic device, fine measurements of the distance and angle between the penetration point and target area can be difficult and imprecise. Using the holes in the penetration grid as a visible fiducial MRI marker helps mitigate this problem (**Fig. 5**). Specifically, the penetration grid can be filled with a contrast agent such as povidone-iodine ointment (**Fig. 5A**), making it visible in the MRI. In some cases, such as targeting small or deep structures, particularly precise estimates of the probe trajectory may be required. Such estimates can be made using a specialized grid (**Fig. 5B**). This grid has the same shape and guide hole configuration as the penetration grid but is thicker (10 vs. 5 mm) and contains four hollow pillars that are perpendicular to the grid surface. By filling this grid and the pillars with a contrast agent, these features can aid in making more precise estimates of penetration trajectories. As illustrated in **Fig. 5C**-**E**, the fiducial marker provided by the standard penetration grid (**Fig. 5A**) can also be used to estimate the probe's trajectory (Kalwani et al., 2009; Dubowitz & Scadeng, 2011; Glud et al., 2017). Here, the structural MRIs were rotated and aligned to the horizontal plane of the penetration grid using 3DSlicer (Kikinis et al., 2014). In this way, penetration trajectories can be determined in a simple coordinate system defined by the penetration grid. As shown in the Results, we tested the microdrive by delivering EM to the striatum during an fMRI session. The penetration hole that we used is marked in **Fig. 5C** (black crosshair) and the trajectory is shown on the rotated coronal and sagittal MRI sections in **Fig. 5D**,**E** (orange line), respectively.

295
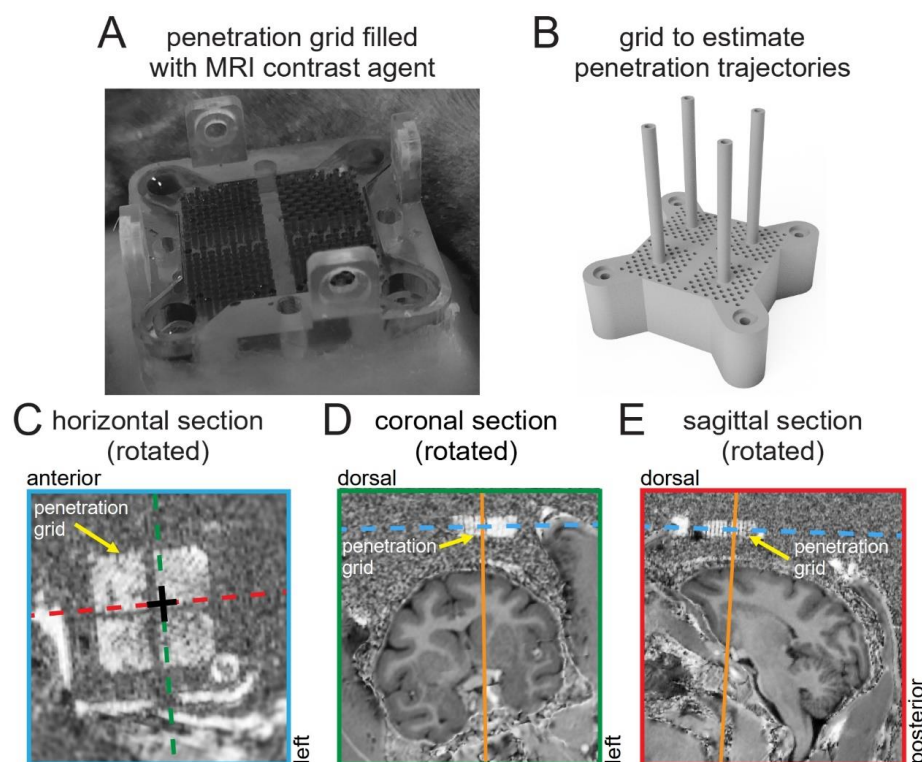
Figure 5. Estimating trajectories using the penetration grid. ***A***, Picture of the penetration grid secured to the implant and filled with an MRI contrast agent (povidone-iodine ointment). ***B****,* 3D rendering of a specialized grid for making precise estimates of penetration trajectories. This grid has the same pattern of penetration holes as the standard penetration grid (***A***), but is thicker (10 mm, compared to 5 mm) and has four hollow pillars which are perpendicular to the grid surface for filling with an MRI contrast agent. These features can aid in the estimation of penetration trajectories. ***C***-***E***, Rotated MRI sections aligned relative to the horizontal plane of the penetration grid shown in ***A***. ***C***, Rotated horizontal MRI section providing a top-down view of the penetration grid. The four quadrants of the grid are visible and the penetration hole used in testing the microdrive is marked (black crosshair) along with the rotated coronal (green dashed line) and rotated sagittal (red dashed line) MRI sections. ***D***, Rotated coronal MRI section aligned relative to the horizontal plane defined by the penetration grid (blue dashed line), showing the estimated penetration trajectory (orange line). Note that the penetration trajectory is perpendicular to the horizontal plane of the penetration grid. ***E***, Same as ***D*** but for the rotated sagittal MRI section.

Preparation of the microdrive assembly and its installation

After identifying the desired penetration hole, a micro-drilling technique is used to create a minimum opening through the cranium (here, ϕ0.7 mm; Ideal Micro-Drill, Harvard Apparatus, Inc.; **Fig. 6A**). To start, the acrylic layer within the implant is cleaned. The penetration grid is then cleaned with isopropyl alcohol and installed on the implant. A sterilized drill bit with a drill

317   stop collar is then prepared with a bore depth that is slightly longer (e.g., 1 mm) than the
318   thickness of the penetration grid (here, 5 mm). The top of the penetration grid serves as a
319   reference for determining drilling depths and guide tube lengths. After the initial drilling, the drill
320   bit length is sequentially incremented (e.g., in 1 mm steps) until it passes through the cranium.
321   Before engaging the drill, a subsequent drill bit is first used to hand-verify if the previous bit
322   passed through the cranium. Specifically, the drill bit is lowered through the penetration grid until
323   one of two possibilities occur. If the bit stops before the drill stop collar contacts the penetration
324   grid, then the previous bit did not pass through the cranium and drilling should continue. If the
325   drill bit lowers until the drill stop collar contacts the penetration grid, then the previous drill bit
326   passed through the cranium and drilling should cease. The bore depth that passed through the
327   cranium is used to determine the guide tube length. The guide tube should be slightly longer
328   than the final drill bit plus the distance from the top of the penetration grid to the top of the
329   stopper. In that case, when the guide tube and microdrive body assembly are installed
330   (described below), the guide tube punctures the dura but minimally impinges on the brain.

331   For MRI studies, guide tubes should be made of a non-metallic material (e.g., silica
332   tubing). However, such materials may not be rigid enough to puncture the dura. This challenge
333   can be overcome by adding an intermediate step in which the dura is punctured using a sterile
334   hypodermic needle. Specifically, the dura can be punctured by preparing and inserting a sterile
335   hypodermic needle that is slightly longer than the final drill bit. After removing the hypodermic
336   needle, a non-metallic guide tube can pass through the opening made in the dura.

337   Once a guide tube is prepared, it is soaked in a cleaning solution and secured (e.g.,
338   using super glue or other high-strength adhesive) to the hole in the stopper that matches the
339   identified hole in the penetration grid (**Fig. 6B**). The guide tube should be flush with the top of
340   the stopper to ensure the intended guide tube length. The probe is then loaded through the
341   guide tube and secured (again using a high-strength adhesive) to the corresponding hole in the
342   coupler (**Fig. 6B**). To independently control multiple probes, this process can be repeated with
343   multiple actuators (up to four in the presented design). Each actuating mechanism is then
344   loaded into a chamber of the microdrive body, sliding it down until the stopper rests upon the
345   stopping notches within the chamber (**Figs. 3B**, **6C**). The loaded actuators are then secured to
346   the microdrive body using the microdrive cap, which attaches to the top of the microdrive body
347   with four Nylon screws (**Figs. 1C**, **4A**). The microdrive body assembly is then ready to be
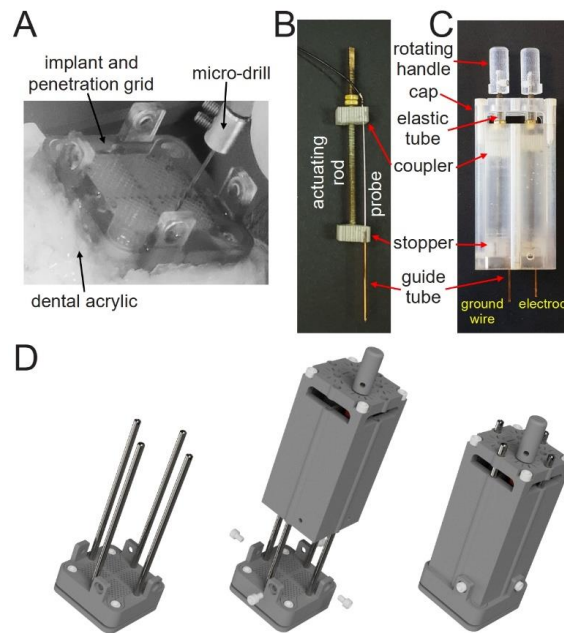348   installed on the implant (**Fig. 6C**).

349

350

Figure 6. Preparing the microdrive body assembly and installing it on the implant. *A*, Micro-drilling through the penetration grid. The implant is secured to an acrylic layer over the cranium. The penetration grid is installed and a micro-drill is used to prepare the penetration site. *B*, Prepared actuating mechanism. Here, a silica guide tube is secured to the stopper and a probe is secured to the coupler. *C*, Prepared microdrive body assembly. Two actuating mechanisms are loaded in two separate chambers of the microdrive body. One actuating mechanism positions the ground wire (left) and the other positions the stimulating electrode (right). The microdrive cap is secured to the microdrive body and rotating handles are attached to the actuating rods. *D*, 3D rendering of the installation of the microdrive body assembly onto the implant. *Left:* Four guide rods are installed on the implant. *Middle:* The prepared microdrive body assembly slides onto the four guide rods. *Right:* The microdrive body assembly is slowly lowered down onto the implant. Once in place, the microdrive body assembly is secured with four Nylon screws and the guide rods can be removed.

364

Before installing the microdrive body assembly, four guide rods are screwed into the edges of the implant (**Figs. 2A**,**B**, **6D** left). The guide rods are used to align the microdrive body with the implant and penetration grid, ensuring that the guide tubes and probes (secured to stoppers and couplers, respectively) maintain alignment with the prepared penetration holes. The aligned microdrive body assembly is then slowly slid down the guide rods towards the implant while monitoring that the tips of the guide tubes enter the appropriate holes in the penetration grid (**Fig. 6D** middle). Once the microdrive is fully lowered, it is secured to the implant with four Nylon screws (**Fig. 6D** right). After this setup is complete, a probe can be manually lowered/raised by rotating the actuating rod via the rotating handle. To use the

14

374 microdrive in an MRI study, the guide rods are unscrewed and removed through the top of the
375 microdrive cap before scanning to prevent imaging artifacts.

376 If using an electrode, a direct connection to a head stage amplifier can be made with
377 electrical wires. For stereotrodes or tetrodes, an additional electrical interface board can be
378 attached to the top of the microdrive body (not shown here but included with the CAD files).

379

380 **Experimental procedures**
381 All procedures were approved by the IACUC at Sungkyunkwan University (SKKUIACUC2019-
382 03-11-1) and were in accordance with the NIH Guide for the Care and Use of Laboratory
383 Animals. An adult male rhesus monkey (*Macaca mulatta*; weight: 10 kg; age: 7 years) was
384 implanted with an MRI-compatible round-shaped PEEK headpost (Micro Integration Technology)
385 that was secured using ceramic screws (Thomas Recording) and dental acrylic (Unifast Trad).
386 The microdrive implant was secured to a layer of acrylic over the cranium. A post-surgical
387 structural scan was used to confirm the location of the implant and to estimate the penetration
388 trajectory (**Fig. 5**).

389

390 **MRI scanning preparation**
391 Based on the estimated trajectory (**Fig. 5**), the penetration grid was used as a guide to drill two
392 holes through the cranium. One hole was for a stimulating electrode and the other was for a
393 ground wire (**Fig. 6A**). Sterile hypodermic needles were then used to puncture corresponding
394 holes in the dura. A stimulating electrode and ground wire were prepared and loaded into fused
395 silica guide tubes (OD: 666 μm, ID: 449 μm; Polymicro) that were secured to separate actuating
396 mechanisms (**Fig. 6B**,**C**). The microdrive body assembly was then installed on the implant and
397 secured using Nylon screws (**Fig. 6D**). During the EM session, no contrast agent was applied to
398 the implant or penetration grid. Finally, the stimulating electrode was lowered into the brain and
399 the ground wire was lowered into the epidural space.

400 MRI images were acquired under anesthesia (isoflurane, ~1–1.2%). The electrode
401 trajectory was confirmed with structural and blood oxygenation level dependent (BOLD) imaging
402 (**Fig. 7A**,**B**) before the injection of MION (10 mg/kg; total MION = 100 mg; Biopal).
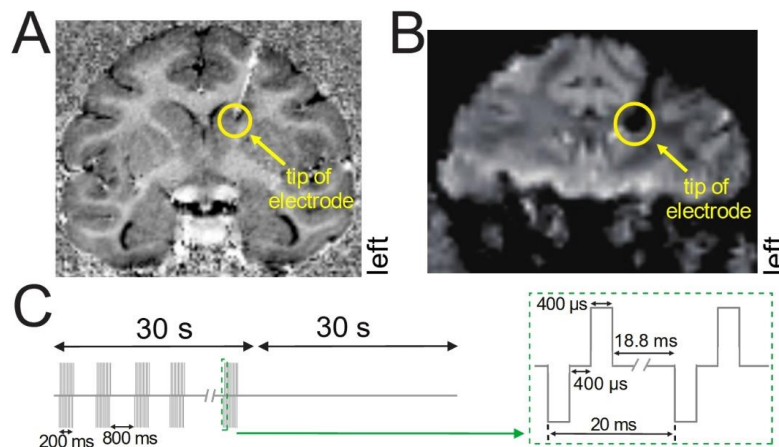
403

Figure 7. Electrode trajectory and EM schematic. *A*, Coronal section from a structural scan with the electrode tip in the caudate nucleus. The electrode is visible as a black line and a metal-induced susceptibility artifact (white). The yellow circle marks the location of the electrode tip. Note that the microdrive caused little-to-no image distortion, even directly below the implant (above where the electrode enters the brain). *B*, Coronal section from a BOLD scan averaged over 540 repetitions with the electrode in place. The electrode (here, a black artifact) and tip (yellow circle) are visible but relatively little distortion from the microdrive is apparent. *C*, Schematic of the EM schedule. A train of 400 μs square waves (500 μA) at 50 Hz lasting 200 ms was delivered every 1000 ms (800 ms spacing) for 30 s. Periods of stimulation (30 s) and no stimulation (30 s) were interleaved.

fMRI scanning

Experiments were conducted using a 7T MRI scanner (Terra, Siemens Healthineers) with a 28-channel knee coil (inner diameter, 15.4 cm). Structural images were acquired using a magnetization-prepared 2 rapid acquisition gradient echoes (MP2RAGE) sequence (TR = 4.3 s; TE = 2.12 ms; slice thickness = 0.5 mm iso). BOLD and MION-enhanced CBV data were collected using a gradient-echo echo planar imaging (GRE-EPI) sequence (TR = 1.5 s; TE = 20 ms; slice thickness = 0.9 mm iso; 52 slices) with whole-brain coverage.

Electrodes and EM plan

Two 231 μm diameter Platinum-Iridium electrodes (exposed tip diameter ~2-3 μm; MicroProbes) were used for stimulation (impedance = 30 kΩ) and grounding (impedance ≤ 500 Ω). Electrical impulses were generated by a stimulator with two isolators (Master-9 and ISO-Flex stimulus isolator, A.M.P.I) to apply biphasic current pulses. Each EM block was triggered and synchronized with the scanning procedures by TTL signals from the MRI scanner (MATLAB, MathWorks, Inc.). Stimulation consisted of trains of biphasic cathode-leading currents with a

431 pulse width of 400 μs and a current of 500 μA, repeated at 50 Hz (**Fig. 7C** right). Stimulation
432 trains lasted 200 ms and were repeated every second for 30 s. Periods of 30 s of stimulation
433 and 30 s of no stimulation were interleaved (**Fig. 7C** left). Each stimulation session consisted of
434 13 blocks (i.e., 13 periods of stimulation and 13 periods of no stimulation interleaved).

435

436 **Image processing and data analysis**
437 Analyses were performed using MATLAB and the Canlab SPM-based fMRI toolboxes
438 (https://github.com/canlab/CanlabCore) (Woo et al., 2017). Structural images were calculated
439 using the following equation:

440
$$I = Real\left(\frac{A^* \cdot B}{|A|^2 + |B|^2}\right),$$
equation 1

441

442 where A is the first inversion contrast image, A^* is the complex conjugate of A, B is the second
443 contrast image from the MP2RAGE sequence, and $|\cdot|$ denotes absolute value (Marques et al.,
444 2010). This method improves the contrast of the brain, but also increases noise outside of the
445 brain as well as metal-induced susceptibility artifacts (**Fig. 7A**). Structural images were then co-
446 registered to the mean functional images, reoriented to the D99 atlas (Reveley et al., 2017), and
447 segmented into gray and white matter. Functional images were re-oriented using the
448 reorientation matrix obtained from the structural re-orientating process. The images were then
449 motion-corrected, normalized, and smoothed with a Gaussian kernel (1.0 mm full-width at half-
450 maximum). High-pass filtering (cut-off frequency = 0.008 Hz) was used to remove low-frequency
451 signal drifts from the fMRI time series. The CBV signal was then inverted because an increase
452 in blood volume lowers the signal and darkens the image intensity.

453 Activation maps based on average CBV measurements across stimulation blocks were
454 constructed using a general linear model (GLM) with a design matrix that included a regressor
455 for the EM by convolving the stimulation profile with a boxcar hemodynamic response function.
456 Head movement parameters were accounted for by including linear and quadratic realignment
457 parameters based on current and previous volumes. Statistical maps were then overlaid on the
458 D99 monkey brain atlas to show the areas activated by EM. Voxel-wise t-contrast activations on
459 the spatial maps (false discovery rate, q < 0.05) were used to determine significant activations.
460 The temporal pattern of the CBV response for each stimulation block was constructed by
461 averaging CBV time courses across all voxels within a region of interest (ROI) that had GLM
462 beta values greater than 6 (corresponding to the 80th percentile of non-zero beta values across
463 all analyzed regions). Voxels belonging to an ROI were determined using the D99 atlas.
464 Activations were reported as percent signal change.

Results

To test the functionality of the microdrive, we used it to deliver EM to the dorsal caudate nucleus (dCN), ventral caudate nucleus (vCN), and nucleus accumbens (NA) of a male macaque monkey in an EM-coupled 7T fMRI study. Structural and BOLD images were periodically taken while lowering the electrode into these areas in order to verify the electrode's location (**Fig. 7A**,**B**). Importantly, we found that the microdrive generated minimal imaging artifacts in the structural scan, even directly below the implant (**Fig. 7A**). Even in the BOLD images, which are more vulnerable to artifacts than structural images (Murakami et al., 2016), there was relatively little image distortion from the microdrive (**Fig. 7B**). The penetration grid was not visible in these images because it was not filled with a contrast agent during the EM session. As expected, the electrode was visible in both the structural and BOLD scans (**Fig. 7A**,**B**, respectively). It appears as a white metal-induced susceptibility artifact in the structural image that is more prominent after the calculation of the structural image from the MP2RAGE scans (**Eq. 1**). Importantly, these images confirm that the microdrive itself introduced minimal imaging artifacts, even at 7T, making it possible to monitor the position of the probe with a high degree of accuracy.
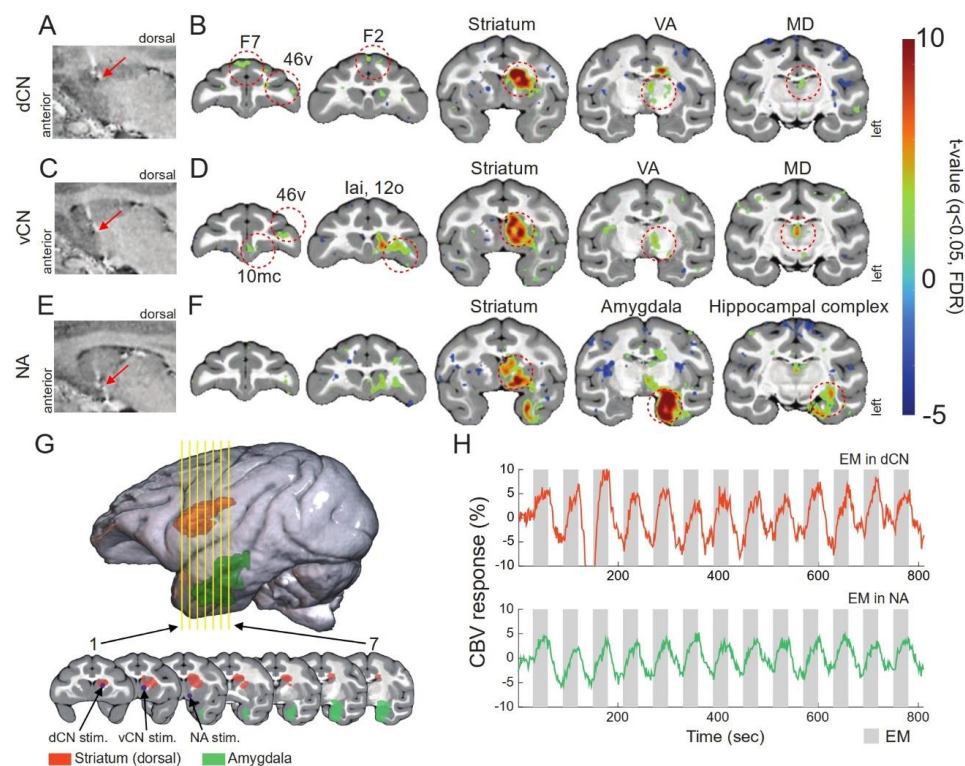
Figure 8. Activation maps and temporal patterns of CBV during EM. *A*, Location of the first stimulation site (dCN, red arrow) on a sagittal view. *B*, Activation maps during dCN EM overlaid on the D99 atlas with ROIs outlined and labeled (red circles). *C*, Location of the second stimulation site (vCN, red arrow) on a sagittal view. *D*, Activation maps during vCN EM overlaid on the D99 atlas with ROIs outlined and labeled (red circles). *E*, Location of the third stimulation site (NA, red arrow) on a sagittal view. *F*, Activation maps during NA EM overlaid on the D99 atlas with ROIs outlined and labeled (red circles). *G*, 3D rendering of the D99 atlas (top) with two ROIs colored (orange: dorsal striatum; green: amygdala). Seven coronal sections are also shown (bottom; yellow lines from top). On sections 1, 2, and 3, purple dots and black arrows mark the dCN, vCN, and NA stimulation sites, respectively. *H*, Time-course of percent signal change (colored lines) measured in the dorsal striatum during EM in the dCN (top) and amygdala during EM in the NA (bottom). Gray bars indicate 30 s stimulation periods and white bars indicate 30 s no stimulation periods (all 13 blocks are shown). To facilitate comparisons, the time courses are plotted with the same ordinate range. This results in some clipping in the top trace. Abbreviations: dCN, dorsal caudate nucleus; vCN, ventral caudate nucleus; NA, nucleus accumbens; F2, agranular frontal area F2; F7, agranular frontal area F7; 12o, orbital prefrontal area; 46v, ventro-lateral prefrontal area; 10mc, medial prefrontal area; Iai, intermediate agranular insula area; MD, mediodorsal thalamus; VA, ventral anterior thalamus.

To assess the effects of EM delivered using the microdrive, we applied EM at three locations in the left hemisphere: the dCN, vCN, and NA. At each location, 13 blocks of EM were delivered. The resulting activation maps are shown in **Fig. 8**. We first stimulated the dCN (penetration depth from the dura = 13.14 mm; **Fig. 8A** red arrow) and found that activity significantly increased in the ipsilateral striatum, agranular frontal area F2, ventro-lateral prefrontal area (46v), mediodorsal thalamus (MD), and ventral anterior thalamus (VA; **Fig. 8B**). A significant increase in activity was also observed in the contralateral agranular frontal area F7. In the same imaging session, we lowered the stimulating electrode into the vCN (penetration depth from the dura = 18.57 mm; **Fig. 8C** red arrow). During EM of the vCN, we found that activity significantly increased in the ipsilateral striatum, 46v, MD, VA, medial prefrontal area (10mc), intermediate agranular insula area (Iai), and orbital prefrontal area (12o; **Fig. 8D**). The observed activations associated with dCN and vCN EM were consistent with the known anatomical connectivity of the striatum (McFarland & Haber, 2002; Haber, 2016). Lastly, we lowered the stimulating electrode into the NA (penetration depth from the dura = 22.88 mm; **Fig. 8E** red arrow). During EM of the NA, we found that activity significantly increased in the ipsilateral striatum, amygdala, and hippocampal complex (**Fig. 8F**). These observed activations were consistent with the known anatomical connectivity of the NA (Alexander et al., 1986; Friedman et al., 2002; Choi et al., 2017).

To confirm that the temporal pattern of the CBV responses followed the EM schedule, we calculated the time course of activation in select ROIs during dCN and NA stimulation. For stimulation of the dCN, we calculated the activity within the dorsal striatum, which included the

522   stimulation site (**Fig. 8G**,**H** orange). For stimulation of the NA, we calculated the activity within
523   the relatively distal amygdala (**Fig. 8G**,**H** green). In both cases, the pattern of activity was robust
524   and temporally locked to the EM schedule, with the signal increasing after the onset of
525   stimulation (**Fig. 8H** gray bars) and decreasing after stimulation ceased (**Fig. 8H** white bars).
526   These results confirm that the MRI compatible microdrive could be used to reliably deliver EM to
527   designated brain areas in a 7T MRI environment with minimal imaging artifacts.
528

529   **Discussion**

530   For many neuroscience experiments, the microdrive is an essential nexus between neuronal
531   activity and data acquisition. To satisfy the specific demands of a study, it is often necessary to
532   customize the microdrive's design to ensure accurate and reliable control of probes. Such
533   customization introduces additional development time and manufacturing costs, particularly
534   when it relies on conventional machining. A potentially more effective approach to customizing
535   microdrives is to utilize 3D printing capabilities with sub-millimeter resolution. Indeed, the utility
536   of 3D printing has recently become apparent across a wide range of research and medical
537   applications (Liaw & Guvendiren, 2017; Jamróz et al., 2018; Nagarajan et al., 2018).

538   Here we demonstrated the feasibility of using a 3D printed, MRI compatible microdrive in
539   an EM-coupled fMRI study. We found that the workflow from design to CAD to fabrication with
540   3D printing was seamless, and that 3D printing was especially efficient for constructing the
541   microdrive's small components. This advantage can further expedite customization. For
542   example, the presented design includes four chambers to accommodate four independent
543   actuators, but the supplied CAD files can be easily modified to print a microdrive body that
544   houses fewer or more actuators depending on the number of target areas and the brain size.
545   The length of the chamber can also be easily modified to accommodate shorter or longer travel
546   distances. Importantly, the simplicity of the workflow can support an almost immediate response
547   to new experimental demands, which is not always possible with commercial manufacturers.
548

549   **Micro-drilling reduces imaging artifacts and implant maintenance**

550   The microdrive produced no substantial imaging artifacts because it was made of MRI
551   compatible materials and few metallic parts. In addition, the use of a penetration grid and micro-
552   drilling technique eliminated the need for a larger craniotomy and conventional chamber which
553   can create an air-filled space that is problematic for imaging and can potentially result in
554   deformation of the underlying neural tissue. To minimize damage to the dura and neural tissue
555   during micro-drilling, a drill stop collar was used to ensure precise control of the bore depth. By

556 hand-verifying the bore depth, it is possible to determine the drill bit length that passes through
557 the cranium within the tolerance of the step size that the drill bits are incremented (e.g., 1 mm).
558 We have used variations of this technique for years (Rosenberg et al., 2013; Laurens et al.,
559 2016; Chang et al., 2020), and have not encountered problems with infection. Meticulous
560 cleaning of the acrylic layer before and after drilling, cleaning and sterilizing components, and
561 covering the implant outside of the experiment (CAD files for a cover are provided but not
562 shown) greatly reduce the risk of infection. However, if infection occurs, the local acrylic layer
563 could be removed and the infection treated topically. The acrylic layer could then be replaced.
564 Thus, the micro-drilling technique helps reduce imaging artifacts associated with larger
565 craniotomies as well as implant maintenance.

566

567 **Performance of the microdrive during EM-coupled MRI scanning**

568 The microdrive showed excellent performance in a 7T MRI environment where it was used to
569 position a stimulating electrode and deliver EM. We placed the electrode in the dCN, vCN, and
570 NA, and delivered EM during fMRI scanning to assess the effective connectivity of these areas
571 across the brain. For each stimulation location, we found that the induced activation was largely
572 restricted to the ipsilateral side of the brain, consistent with some previous findings (Tolias et al.,
573 2005; Matsui et al., 2011). However, it is also possible that our imaging methods limited the
574 ability to detect contralateral activations. Indeed, other studies have shown some contralateral
575 activations induced by EM, consistent with anatomical connections across hemispheres
576 (Ekstrom et al., 2008; Moeller et al., 2008; Premereur et al., 2015; Murris et al., 2020). As
577 expected for the EM of striatal regions, the activated areas were known constituents of the basal
578 ganglia circuit (Draganski et al., 2008; Haber & Knutson, 2010). The results thus confirmed that
579 our MRI compatible and 3D printed microdrive can be used to examine the connectivity of brain
580 networks using EM-coupled whole-brain imaging.

581

582 **Future applications and current limitations**

583 Here we demonstrated the feasibility of using our 3D printed microdrive in an EM-coupled fMRI
584 study. Due to the versatile design of the actuating mechanism, the microdrive can
585 accommodate various types of electrodes for neuronal recordings (e.g., linear arrays,
586 stereotrodes, or tetrodes), cannulae for inactivation or neuropharmacological studies, or
587 optogenetic fibers for precise neuronal modulation. Thus, the microdrive can support a wide
588 range of future applications. In the current design, a probe is advanced by manually rotating an
589 actuating rod. However, studies often require a period in which the probe must be moved

590 frequently while continuously monitoring neuronal activity (e.g., while approaching a target brain
591 area). In such cases, a motorized actuating module would be more efficient than the current
592 manual mechanism. We therefore have plans to incorporate a motorized actuating module with
593 control software as an extension of the existing design. Lastly, our skull-mounted frameless
594 design is potentially suitable as a chronic microdrive for longer-term applications. The future
595 addition of a protective housing could enable the microdrive body to stay attached to the implant
596 for an extended period of time, potentially with freely moving animals (Wilson et al., 2003;
597 Greenberg & Wilson, 2004; Sun et al., 2006).

598 The CAD files and a parts list for the MRI compatible microdrive are available here:
599 https://osf.io/tnpmk/. We encourage others to make modifications based on their specific
600 research needs and hope that our designs facilitate neuroscience research by reducing the time
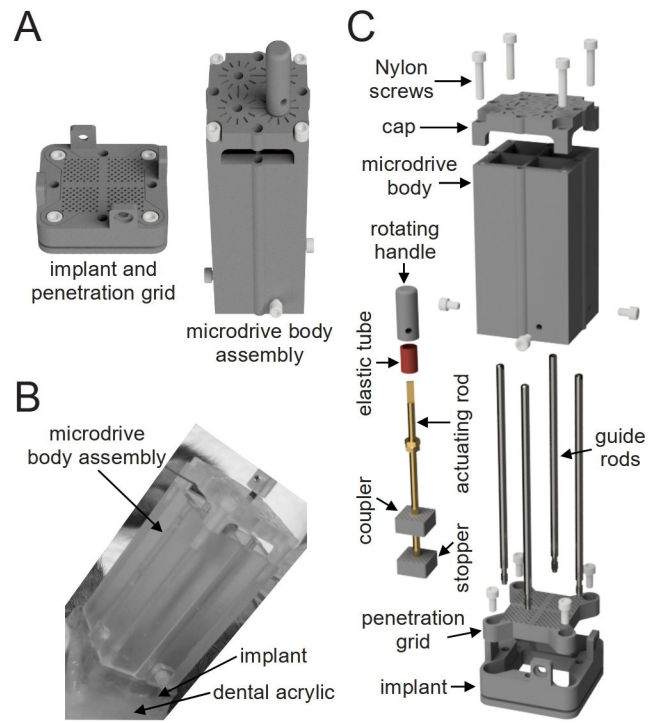601 and effort necessary to solve microdrive-related technical issues.
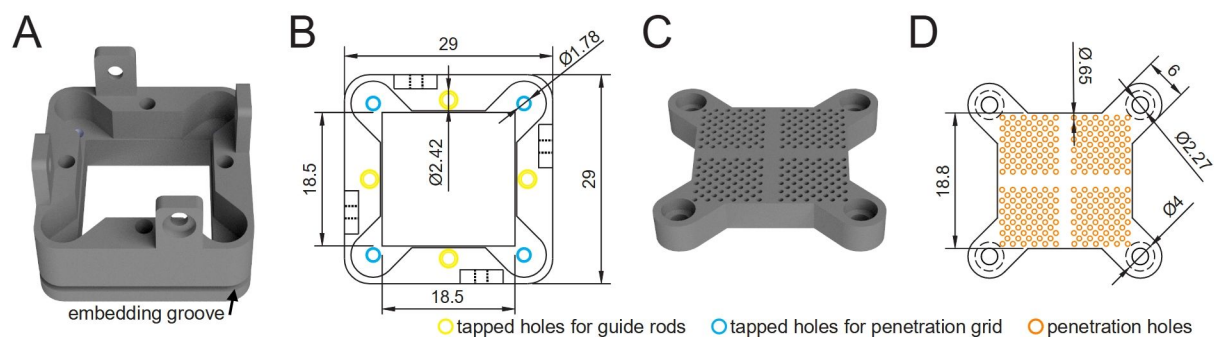
602

603 **References**
604 Alexander, G. E., DeLong, M. R., & Strick, P. L. (1986). Parallel organization of functionally
605 segregated circuits linking basal ganglia and cortex. *Annual Review of Neuroscience*, *9*, 357–
606 381. https://doi.org/10.1146/annurev.ne.09.030186.002041
607 Chang, T.-Y., Doudlah, R., Kim, B., Sunkara, A., Thompson, L. W., Lowe, M. E., & Rosenberg,
608 A. (2020). Functional links between sensory representations, choice activity, and
609 sensorimotor associations in parietal cortex. *eLife*, *9*, e57968.
610 https://doi.org/10.7554/eLife.57968
611 Choi, E. Y., Ding, S.-L., & Haber, S. N. (2017). Combinatorial Inputs to the Ventral Striatum from
612 the Temporal Cortex, Frontal Cortex, and Amygdala: Implications for Segmenting the
613 Striatum. *ENeuro*, *4*(6). https://doi.org/10.1523/ENEURO.0392-17.2017
614 Dotson, N. M., Hoffman, S. J., Goodell, B., & Gray, C. M. (2017). A Large-Scale Semi-Chronic
615 Microdrive Recording System for Non-Human Primates. *Neuron*, *96*(4), 769-782.e2.
616 https://doi.org/10.1016/j.neuron.2017.09.050
617 Draganski, B., Kherif, F., Klöppel, S., Cook, P. A., Alexander, D. C., Parker, G. J. M.,
618 Deichmann, R., Ashburner, J., & Frackowiak, R. S. J. (2008). Evidence for segregated and
619 integrative connectivity patterns in the human Basal Ganglia. *The Journal of Neuroscience:*
620 *The Official Journal of the Society for Neuroscience*, *28*(28), 7143–7152.
621 https://doi.org/10.1523/JNEUROSCI.1486-08.2008
622 Dromme, I. C. V., Premereur, E., Verhoef, B.-E., Vanduffel, W., & Janssen, P. (2016). Posterior
623 Parietal Cortex Drives Inferotemporal Activations During Three-Dimensional Object Vision.
624 *PLOS Biology*, *14*(4), e1002445. https://doi.org/10.1371/journal.pbio.1002445
625 Dubowitz, D. J., & Scadeng, M. (2011). A frameless stereotaxic MRI technique for macaque
626 neuroscience studies. *The Open Neuroimaging Journal*, *5*, 198–205.
627 https://doi.org/10.2174/1874440001105010198
628 Duffau, H. (2020). What Direct Electrostimulation of the Brain Taught Us About the Human
629 Connectome: A Three-Level Model of Neural Disruption. *Frontiers in Human Neuroscience*,
630 *14*. https://doi.org/10.3389/fnhum.2020.00315
631 Ekstrom, L. B., Roelfsema, P. R., Arsenault, J. T., Bonmassar, G., & Vanduffel, W. (2008).
632 Bottom-up dependent gating of frontal signals in early visual cortex. *Science (New York,*
633 *N.Y.)*, *321*(5887), 414–417. https://doi.org/10.1126/science.1153276
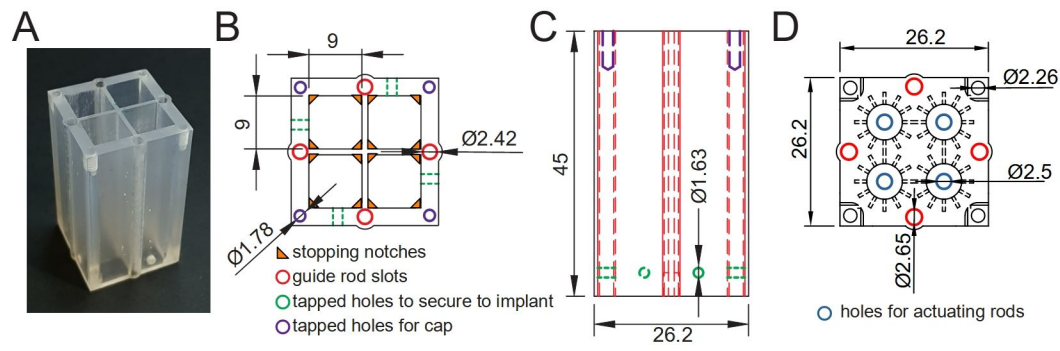
634 Friedman, D. P., Aggleton, J. P., & Saunders, R. C. (2002). Comparison of hippocampal,
635   amygdala, and perirhinal projections to the nucleus accumbens: Combined anterograde and
636   retrograde tracing study in the Macaque brain. *The Journal of Comparative Neurology*,
637   *450*(4), 345–365. https://doi.org/10.1002/cne.10336
638 Glud, A. N., Bech, J., Tvilling, L., Zaer, H., Orlowski, D., Fitting, L. M., Ziedler, D., Geneser, M.,
639   Sangill, R., Alstrup, A. K. O., Bjarkam, C. R., & Sørensen, J. C. H. (2017). A fiducial skull
640   marker for precise MRI-based stereotaxic surgery in large animal models. *Journal of*
641   *Neuroscience Methods*, *285*, 45–48. https://doi.org/10.1016/j.jneumeth.2017.04.017
642 Grahn, P. J., Goerss, S. J., Lujan, J. L., Mallory, G. W., Kall, B. A., Mendez, A. A., Trevathan, J.
643   K., Felmlee, J. P., Bennet, K. E., & Lee, K. H. (2016). MRI-Guided Stereotactic System for
644   Delivery of Intraspinal Microstimulation. *Spine*, *41*(13), E806.
645   https://doi.org/10.1097/BRS.0000000000001397
646 Greenberg, P. A., & Wilson, F. A. W. (2004). Functional stability of dorsolateral prefrontal
647   neurons. *Journal of Neurophysiology*, *92*(2), 1042–1055.
648   https://doi.org/10.1152/jn.00062.2004
649 Haber, S. N. (2016). Corticostriatal circuitry. *Dialogues in Clinical Neuroscience*, *18*(1), 7.
650 Haber, S. N., & Knutson, B. (2010). The reward circuit: Linking primate anatomy and human
651   imaging. *Neuropsychopharmacology: Official Publication of the American College of*
652   *Neuropsychopharmacology*, *35*(1), 4–26. https://doi.org/10.1038/npp.2009.129
653 Jamróz, W., Szafraniec, J., Kurek, M., & Jachowicz, R. (2018). 3D Printing in Pharmaceutical
654   and Medical Applications—Recent Achievements and Challenges. *Pharmaceutical Research*,
655   *35*(9), 176. https://doi.org/10.1007/s11095-018-2454-x
656 Kalwani, R. M., Bloy, L., Elliott, M. A., & Gold, J. I. (2009). A method for localizing
657   microelectrode trajectories in the macaque brain using MRI. *Journal of Neuroscience*
658   *Methods*, *176*(2), 104–111. https://doi.org/10.1016/j.jneumeth.2008.08.034
659 Kern, T. A., Rörup, H., Werthschützky, R., & Tammer, R. (2008). A remotely controlled
660   lightweight MRI compatible ultrasonic actuator for micrometer positioning of electrodes during
661   neuroethological primate research / Telemetrisch gesteuerter, MRT-kompatibler
662   Ultraschallaktor zur Mikrometerpositionierung von Elektroden in der neuroethologischen
663   Primaten-Forschung. *Biomedical Engineering / Biomedizinische Technik*, *53*(6), 292–299.
664   https://doi.org/10.1515/BMT.2008.046
665 Kikinis, R., Pieper, S. D., & Vosburgh, K. G. (2014). 3D Slicer: A Platform for Subject-Specific
666   Image Analysis, Visualization, and Clinical Support. In F. A. Jolesz (Ed.), *Intraoperative*
667   *Imaging and Image-Guided Therapy* (pp. 277–289). Springer. https://doi.org/10.1007/978-1-
668   4614-7657-3_19
669 Kim, S.-G., Harel, N., Jin, T., Kim, T., Lee, P., & Zhao, F. (2013). Cerebral blood volume MRI
670   with intravascular superparamagnetic iron oxide nanoparticles. *NMR in Biomedicine*, *26*(8),
671   949–962. https://doi.org/10.1002/nbm.2885
672 Kourtzi, Z., Tolias, A. S., Altmann, C. F., Augath, M., & Logothetis, N. K. (2003). Integration of
673   Local Features into Global Shapes: Monkey and Human fMRI Studies. *Neuron*, *37*(2), 333–
674   346. https://doi.org/10.1016/S0896-6273(02)01174-1
675 Laurens, J., Kim, B., Dickman, J. D., & Angelaki, D. E. (2016). Gravity orientation tuning in
676   macaque anterior thalamus. *Nature Neuroscience*, *19*(12), 1566–1568.
677   https://doi.org/10.1038/nn.4423
678 Liaw, C.-Y., & Guvendiren, M. (2017). Current and emerging applications of 3D printing in
679   medicine. *Biofabrication*, *9*(2), 024102. https://doi.org/10.1088/1758-5090/aa7279
680 Logothetis, N. (2003). MR imaging in the non-human primate: Studies of function and of
681   dynamic connectivity. *Current Opinion in Neurobiology*, *13*(5), 630–642.
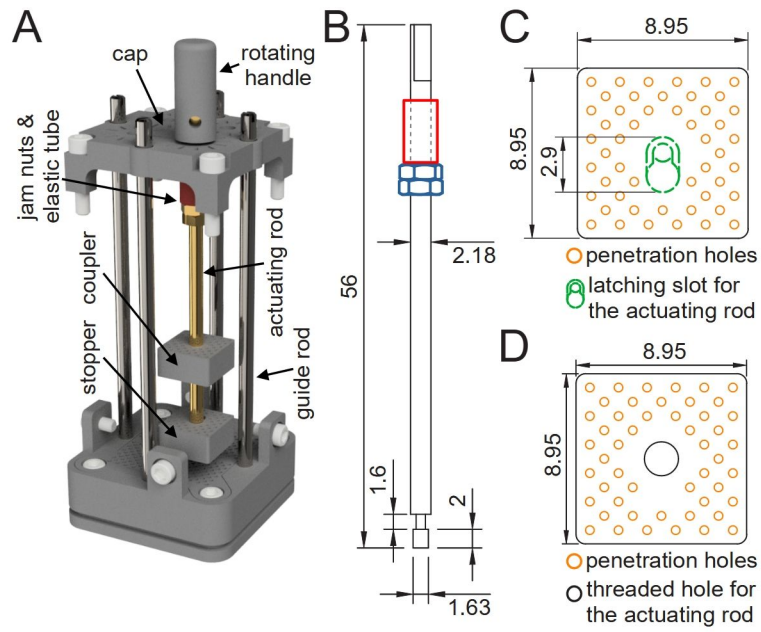682   https://doi.org/10.1016/j.conb.2003.09.017

683   Logothetis, N. K., Augath, M., Murayama, Y., Rauch, A., Sultan, F., Goense, J., Oeltermann, A.,
684   & Merkle, H. (2010). The effects of electrical microstimulation on cortical signal propagation.
685   *Nature Neuroscience*, *13*(10), 1283–1291. https://doi.org/10.1038/nn.2631
686   Marques, J. P., Kober, T., Krueger, G., van der Zwaag, W., Van de Moortele, P.-F., & Gruetter,
687   R. (2010). MP2RAGE, a self bias-field corrected sequence for improved segmentation and
688   T1-mapping at high field. *NeuroImage*, *49*(2), 1271–1281.
689   https://doi.org/10.1016/j.neuroimage.2009.10.002
690   Matsui, T., Tamura, K., Koyano, K. W., Takeuchi, D., Adachi, Y., Osada, T., & Miyashita, Y.
691   (2011). Direct Comparison of Spontaneous Functional Connectivity and Effective
692   Connectivity Measured by Intracortical Microstimulation: An fMRI Study in Macaque Monkeys.
693   *Cerebral Cortex*, *21*(10), 2348–2356. https://doi.org/10.1093/cercor/bhr019
694   McFarland, N. R., & Haber, S. N. (2002). Thalamic Relay Nuclei of the Basal Ganglia Form Both
695   Reciprocal and Nonreciprocal Cortical Connections, Linking Multiple Frontal Cortical Areas.
696   *The Journal of Neuroscience*, *22*(18), 8117. https://doi.org/10.1523/JNEUROSCI.22-18-
697   08117.2002
698   McMahon, D. B. T., Bondar, I. V., Afuwape, O. A. T., Ide, D. C., & Leopold, D. A. (2014). One
699   month in the life of a neuron: Longitudinal single-unit electrophysiology in the monkey visual
700   system. *Journal of Neurophysiology*, *112*(7), 1748–1762.
701   https://doi.org/10.1152/jn.00052.2014
702   Milham, M., Petkov, C. I., Margulies, D. S., Schroeder, C. E., Basso, M. A., Belin, P., Fair, D. A.,
703   Fox, A., Kastner, S., Mars, R. B., Messinger, A., Poirier, C., Vanduffel, W., Van Essen, D. C.,
704   Alvand, A., Becker, Y., Ben Hamed, S., Benn, A., Bodin, C., … Zhou, Y. (2020). Accelerating
705   the Evolution of Nonhuman Primate Neuroimaging. *Neuron*, *105*(4), 600–603.
706   https://doi.org/10.1016/j.neuron.2019.12.023
707   Moeller, S., Freiwald, W. A., & Tsao, D. Y. (2008). Patches with links: A unified system for
708   processing faces in the macaque temporal lobe. *Science (New York, N.Y.)*, *320*(5881), 1355–
709   1359. https://doi.org/10.1126/science.1157436
710   Murakami, S., Verdonschot, R. G., Kataoka, M., Kakimoto, N., Shimamoto, H., & Kreiborg, S.
711   (2016). A standardized evaluation of artefacts from metallic compounds during fast MR
712   imaging. *Dentomaxillofacial Radiology*, *45*(8). https://doi.org/10.1259/dmfr.20160094
713   Murris, S. R., Arsenault, J. T., & Vanduffel, W. (2020). Frequency- and State-Dependent
714   Network Effects of Electrical Stimulation Targeting the Ventral Tegmental Area in Macaques.
715   *Cerebral Cortex (New York, N.Y.: 1991)*, *30*(8), 4281–4296.
716   https://doi.org/10.1093/cercor/bhaa007
717   Nagarajan, N., Dupret-Bories, A., Karabulut, E., Zorlutuna, P., & Vrana, N. E. (2018). Enabling
718   personalized implant and controllable biosystem development through 3D printing.
719   *Biotechnology Advances*, *36*(2), 521–533. https://doi.org/10.1016/j.biotechadv.2018.02.004
720   Ogawa, S., & Lee, T. M. (1990). Magnetic resonance imaging of blood vessels at high fields: In
721   vivo and in vitro measurements and image simulation. *Magnetic Resonance in Medicine*,
722   *16*(1), 9–18. https://doi.org/10.1002/mrm.1910160103
723   Premereur, E., Dromme, I. C. V., Romero, M. C., Vanduffel, W., & Janssen, P. (2015). Effective
724   Connectivity of Depth-Structure–Selective Patches in the Lateral Bank of the Macaque
725   Intraparietal Sulcus. *PLOS Biology*, *13*(2), e1002072.
726   https://doi.org/10.1371/journal.pbio.1002072
727   Premereur, E., & Janssen, P. (2020). Effective Connectivity Reveals an Interconnected
728   Inferotemporal Network for Three-Dimensional Structure Processing. *Journal of
729   Neuroscience.* https://doi.org/10.1523/JNEUROSCI.3024-19.2020
730   Reveley, C., Gruslys, A., Ye, F. Q., Glen, D., Samaha, J., E Russ, B., Saad, Z., K Seth, A.,
731   Leopold, D. A., & Saleem, K. S. (2017). Three-Dimensional Digital Template Atlas of the
732   Macaque Brain. *Cerebral Cortex (New York, N.Y.: 1991)*, *27*(9), 4463–4477.
733   https://doi.org/10.1093/cercor/bhw248

734   Rosenberg, A., Cowan, N. J., & Angelaki, D. E. (2013). The visual representation of 3D object
735   orientation in parietal cortex. *The Journal of Neuroscience: The Official Journal of the Society*
736   *for Neuroscience*, *33*(49), 19352–19361. https://doi.org/10.1523/JNEUROSCI.3174-13.2013
737   Spitler, K. M., & Gothard, K. M. (2008). A removable silicone elastomer seal reduces granulation
738   tissue growth and maintains the sterility of recording chambers for primate neurophysiology.
739   *Journal of Neuroscience Methods*, *169*(1), 23–26.
740   https://doi.org/10.1016/j.jneumeth.2007.11.026
741   Sudhakar, V., Mahmoodi, A., Bringas, J. R., Naidoo, J., Kells, A., Samaranch, L., Fiandaca, M.
742   S., & Bankiewicz, K. S. (2019). Development of a novel frameless skull-mounted ball-joint
743   guide array for use in image-guided neurosurgery. *Journal of Neurosurgery*, *132*(2), 595–604.
744   https://doi.org/10.3171/2018.10.JNS182169
745   Sun, N. L., Lei, Y. L., Kim, B.-H., Ryou, J.-W., Ma, Y.-Y., & Wilson, F. A. W. (2006).
746   Neurophysiological recordings in freely moving monkeys. *Methods*, *38*(3), 202–209.
747   https://doi.org/10.1016/j.ymeth.2005.09.018
748   Tolias, A. S., Sultan, F., Augath, M., Oeltermann, A., Tehovnik, E. J., Schiller, P. H., &
749   Logothetis, N. K. (2005). Mapping Cortical Activity Elicited with Electrical Microstimulation
750   Using fMRI in the Macaque. *Neuron*, *48*(6), 901–911.
751   https://doi.org/10.1016/j.neuron.2005.11.034
752   Vanduffel, W., Fize, D., Mandeville, J. B., Nelissen, K., Van Hecke, P., Rosen, B. R., Tootell, R.
753   B., & Orban, G. A. (2001). Visual motion processing investigated using contrast agent-
754   enhanced fMRI in awake behaving monkeys. *Neuron*, *32*(4), 565–577.
755   https://doi.org/10.1016/s0896-6273(01)00502-5
756   Wilson, F. A. W., Ma, Y.-Y., Greenberg, P. A., Ryou, J. W., & Kim, B. H. (2003). A
757   microelectrode drive for long term recording of neurons in freely moving and chaired
758   monkeys. *Journal of Neuroscience Methods*, *127*(1), 49–61. https://doi.org/10.1016/S0165-
759   0270(03)00122-5
760   Wilson, F. A. W., Ryou, J.-W., Kim, B.-H., & Greenberg, P. A. (2005). Amelioration of dural
761   granulation tissue growth for primate neurophysiology. *Journal of Neuroscience Methods*,
762   *144*(2), 203–205. https://doi.org/10.1016/j.jneumeth.2004.11.009
763   Woo, C.-W., Schmidt, L., Krishnan, A., Jepma, M., Roy, M., Lindquist, M. A., Atlas, L. Y., &
764   Wager, T. D. (2017). Quantifying cerebral contributions to pain beyond nociception. *Nature*
765   *Communications*, *8*, 14211. https://doi.org/10.1038/ncomms14211

A
implant and
penetration grid

microdrive body
assembly

B
microdrive
body assembly

implant

dental acrylic

C
Nylon
screws

cap

microdrive
body

rotating
handle

elastic tube

actuating rod

coupler

guide
rods

stopper

penetration
grid

implant

A

embedding groove

B

29
Ø1.78
18.5
Ø2.42
29
18.5

C

D

Ø.65
6
Ø2.27
18.8
Ø4

tapped holes for guide rods   tapped holes for penetration grid   penetration holes

A

B

9

9

Ø2.42

Ø1.78

▲ stopping notches
◯ guide rod slots
◯ tapped holes to secure to implant
◯ tapped holes for cap

C

45

Ø1.63

26.2

D

26.2

26.2

Ø2.26

Ø2.5

Ø2.65

◯ holes for actuating rods

A

cap

rotating handle

jam nuts & elastic tube

actuating rod

stopper coupler

guide rod

B

56

2.18

1.6

2

1.63

C

8.95

8.95

2.9

○ penetration holes

○ latching slot for the actuating rod

D

8.95

8.95

○ penetration holes
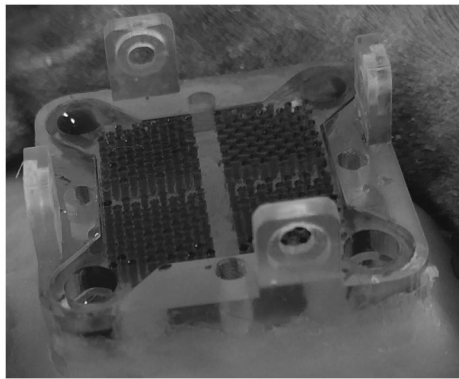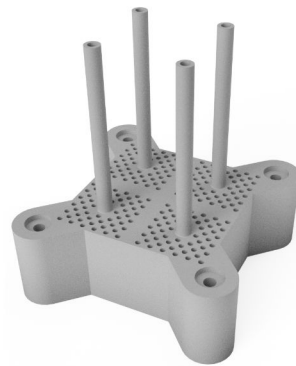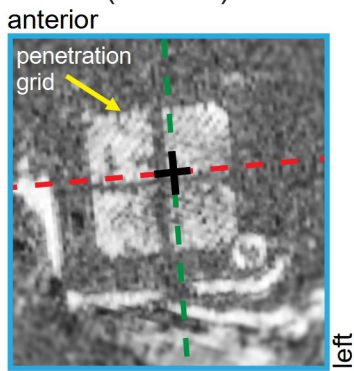
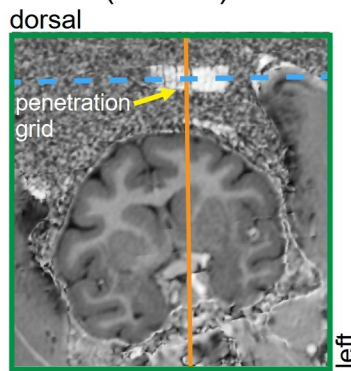○ threaded hole for the actuating rod

A penetration grid filled with MRI contrast agent

B grid to estimate penetration trajectories

C horizontal section (rotated)

anterior

penetration grid

left

D coronal section (rotated)

dorsal

penetration grid

left

E sagittal section (rotated)

dorsal

penetration grid

posterior

A

implant and
penetration grid

micro-drill

dental acrylic

B

actuating
rod

probe

C

rotating
handle

cap

elastic
tube

coupler

stopper

guide
tube

ground
wire

electrode

D

A

tip of
electrode

left

B

tip of
electrode

left

C

30 s   30 s

400 μs

18.8 ms

400 μs

200 ms   800 ms

20 ms